materials

MDPI

Article

Formation of Titanium Carbide MMC and Modelling the Chemical Effect on Powder Density for Additive Manufacturing

Busisiwe J. Mfusi [1,2,*], Ntombizodwa R. Mathe [1,2], Hertzog Bisset [3], Rosinah Modiba [4] and Patricia A. I. Popoola [2]

[1] Photonics Centre, Council for Scientific and Industrial Research, Meiring Naudé Road, Brummeria, Pretoria 0185, South Africa; nmathe@csir.co.za
[2] Chemical, Metallurgical and Materials Engineering Department, Tshwane University of Technology, Staatsartillerie Road, Pretoria West, Pretoria 0183, South Africa; popoolaapi@tut.ac.za
[3] South African Nuclear Energy Corporation SOC Ltd. (Necsa), Elias Motsoaledi Street Extension (Church Street West), R104 Pelindaba, Madibeng Municipality, Brits 0240, South Africa; hertzog.bissett@necsa.co.za
[4] Advanced Materials and Manufacturing, Council for Scientific and Industrial Research, Meiring Naudé Road, Brummeria, Pretoria 0185, South Africa; rmahlangu1@csir.co.za
* Correspondence: mfusibusisiwe08@gmail.com

Abstract

Titanium carbide has developed into an exceptional reinforcement contender in Aluminium Matrix Composites (AMCs) because of its greater characteristics such as elevated hardness, elevated elastic modulus, low heat conductivity, and constancy at moderately elevated temperatures. Furthermore, it is consequently selected as the reinforcing segment in AMCs because of its good thermodynamic and wettability stability inside the aluminium melt pool. In this work, titanium carbide powder was mixed to distinguish $AlSi_{10}Mg$ strengthening by the additive manufacturing (AM) process in the category of powder bed identified as Powder Bed Fusion (PBF). The objective of the study was to have homogeneously mixed powders for processing on the reinforcement of $AlSi_{10}Mg$ with TiC. Different characterisation procedures were carried out, such as scanning electron microscope energy dispersive X-ray spectroscopy (SEM-EDS), pycnometry, and thermogravimetric analysis (TGA). The advancement of powder density from 2.65 to 2.72 g/cm^3 and surface area from 0.02 to 0.14 m^2/g was accomplished. The modelling findings concurred that the addition of Ti and C increases the density of the alloy, with Ti contributing more to AlSi than C. It was deduced that with Ti and C added to the system, the bulk modulus increases, with Al_6Si_8TiC having the largest value of 80.34 GPa.

Keywords: titanium carbide; $AlSi_{10}Mg$; first principle; metal matrix composite; additive manufacturing

Academic Editors: Lehua Liu, Haokai Dong, Haizhou Lu and Chao Zhao

Received: 27 November 2025
Revised: 25 January 2026
Accepted: 30 January 2026
Published: 13 February 2026

1. Introduction

Metal powder-based additive manufacturing (AM) developments are being progressively applied in a variety of productions due to their benefits such as the complexity of the geometry and flexibility of the product, as well as the time effectiveness of these processes, compared to traditional manufacturing processes [1,2]. Currently, the production of operational products with complex geometries, alloy compositions that are diverse, as well as microstructures that are closely regulated, are the reasons these powder-based metal AM procedures have resulted in component manufacturing and not just prototyping [3]. Powder bed fusion (PBF) is one of the AM powder bed classification methods, which is

https://doi.org/10.3390/ma19040715

a layer-by-layer deposition process whereby a thin layer of powder is distributed onto the build plate and the heat from a laser source is applied to melt and fuse the powder into a three-dimensional component [4]. Currently, there is an increasing interest in the advancement of novel innovative materials with desirable characteristics, specifically the use of composite materials, such as Silicon Carbide (SiC) and Titanium Carbide (TiC), to achieve alloys with outstanding characteristics [5–7].

The $AlSi_{10}Mg$ alloy is generally recognised for its resistance to corrosion, conductivity of high heat, good weldability, ability to be casted, and low weight ratio [8]. The application of the $AlSi_{10}Mg$ alloy comprises, but is not limited to, heat exchangers that are subjected to extreme temperatures and conditions that are corrosive [9–11]. With a reputation in the automobile, aerospace, and railway industries, $AlSi_{10}Mg$ is used as a substitute for monolithic counterparts [9]. The SLM-produced $AlSi_{10}Mg$ components have a nearly net shape of almost 100 percent density and a hardness of 128 Hv [12]. The problem begins when thermal treatment is performed with the objective of reducing residual stresses within the component. The structure is disturbed specifically to relieve stress by the movement of silicon from grain boundaries, where it is near-eutectic and agglomerates within the aluminium matrix, causing the structure to soften and lose its nearly ideal mechanical characteristics [9,13]. The existing thermal treatment methods such as stress relief are conventional methods [14]. Thermal treatment techniques suitable for additively manufactured $AlSi_{10}Mg$ have not yet been developed; therefore, a route for applying TiC to strengthen $AlSi_{10}Mg$ is being attempted.

TiC has shown great potential in the hardening and reinforcement of several materials, including titanium, aluminium, and various alloys [15,16]. High-tech disciplines in the aerospace industry, extending from chemical and mechanical engineering to mechanical microelectronics, have been extensively applying TiC in key areas of their disciplines. The extreme melting point, extreme electric conductivity, high wear resistance, high thermal and chemical stability, and elevated hardness are the superior characteristics of titanium carbide [5].

The volume fraction, size, and dispersal of the reinforcement material are not the solitary substantial impacts of the characteristics of the composites, but the relative nature of the matrix that directs the effectiveness of load transmission and the interface between the reinforcement [17,18]. As a result of its best characteristics amongst other ceramic reinforcers, TiC makes an exceptional reinforcement due to its extreme melting point of 3160 °C, high hardness of 40 GPa, low density of 4.9 Kg/dm^3, superior modulus of elasticity of 460 GPa, low heat conductivity coefficient of 15–20 W/m °C, abrasion resistance, extreme shear modulus of 188 GPa, and greater wear resistance [16]. However, even though TiC has been investigated by Munz et al. and Gherrab et al. as an aluminium reinforcement, the former effort has focused on proving that, in terms of strengthening metals, nano-crystal powder particles are actually more operative than micrometre powder particle sizes [19–21].

2. Experimental Procedure

2.1. Materials

The $AlSi_{10}Mg$ and TiC powders were purchased separately from TLS Technik GmbH, Bitterfeld, Germany, and Zhuzhou Jiangwu Boda Hard-facing Material Co., Ltd., Yanling, China, respectively. The $AlSi_{10}Mg$ powder had a spherical morphology and a particle size distribution of 30–65 µm and was used as received [22]. The as-received TiC powder had an irregular morphology and particle size distribution of 30–60 µm. The as-received TiC powder was spheroidized using the TEKSPHERO-15 plasma system at the South African Nuclear Energy Corporation (Necsa), Brits, South Africa.

2.2. Powder Mixing

A Tubular dry chemical laboratory powder mixing machine that uses the concept of shaking to mix the powder was used to mix the spheroidised TiC powder and the $AlSi_{10}Mg$. This mixing system consists of mechanical arms that move and rotate like human arms to shake and mix the powder. The revolving container has one speed and rotates for at least 30 min for efficient powder mixing, which is said to have been optimised. The percentage of 1–5 wt.% TiC was mixed with $AlSi_{10}Mg$ to acquire 100 g of powder for each batch.

2.3. Characterisation Technique

The different-sized powder samples were characterised by the Scanning Electron Microscopy (SEM), using a JEOL JSM 6010 Plus/LA fitted with an Electron Diffraction Spectroscopy (EDS) detector for EDX analysis at a voltage acceleration of 20 kV. X-Ray Diffraction (XRD) was performed using the X'Pert PRO PANalytics X-Ray Diffraction system. The density of the powder was determined using a Micromeritics AccoPys II 1360 pycnometer. Thermogravimetric Analysis (TGA) was performed by means of a Perkin Elmer Pyris 1 TGA analyser, under the conditions of 50 to 900 °C/min for thermogravimetric analysis in a nitrogen atmosphere with preparation of 20 mg powder samples. The BET (Brauner, Emmett and Teller) Surface area analysis was performed using the Micromeritics Tristar II Surface and area porosity analyser fitted with a Micromeritics FlowPrep 060 tube holder, liquid nitrogen-filled dewar elevator and with an installed computer system. Powder moisture was removed by purging the samples with argon gas at 90° before the surface area and porosity analysis.

2.4. First Principles

To enhance the stability of AlSi, the effect of Ti and C on the alloy was investigated. The ab initio density functional theory (DFT) [23,24] formalism as implemented in Cambridge Serial Total Energy Package (CASTEP) [25] with the projector-augmented wave (PAW) [26] was used. For the electronic setup, the energy cutoff and k-point were set to fine. For the functional setup, the generalised gradient approximation of Perdew and Wang (GGA-PBE) [27] was chosen and OTFG ultrasoft (default) for the pseudopotentials. The Brillouin zone integrations were performed for suitably large sets of k-points according to Monkhorst and Pack [28]. The convergence criteria for structure optimisation and energy calculation were set to fine quality with the tolerance for the stress concentration factor (SCF), energy, maximum force and maximum displacement set to 1.0×10^{-5} eV/atom, 0.03 eV/Å, and 0.001 Å, respectively. All the calculations were performed at 0 K. The AlSi was selected for the modelling because of the complexities of making $AlSi_{10}Mg$, which was not in the model. AlSi aids as a representative modelling system for Al-Si alloys to capture important properties while minimising computational demands. The properties captured were the electronic structure, bonding properties, and crystal structure.

3. Results and Discussion

3.1. Microstructural Analysis

Scanning Electron Microscope (SEM) of $AlSi_{10}Mg$ Mixed with TiC Powder

Previous work addressed the properties of the $AlSi_{10}Mg$ powder and its effect on the mechanical characteristics after additive manufacturing [12–14]. One of the drawbacks of additively manufactured aluminium alloys is the loss of strength after conventional thermal treatment [13]. Figure 1a,b present the SEM microstructural images with their EDS spectra for TiC as received and after spheroidization. Figure 2a–e present the SEM microstructural images with their EDS spectra for TiC percentage of 1–5 wt.% mixed into $AlSi_{10}Mg$ powder.

EDS analysis was performed to demonstrate the overall elemental composition of TiC in the $AlSi_{10}Mg$ powder mixture.

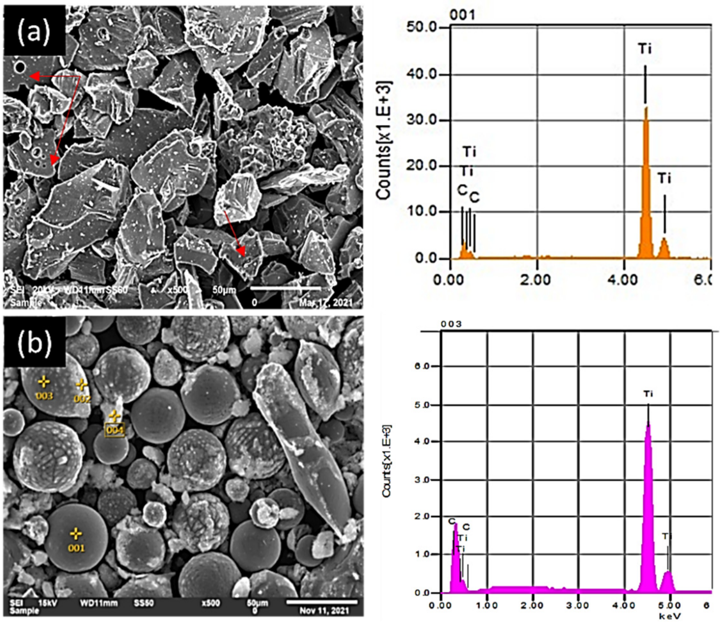

Figure 1. EDS spectra of the (**a**) unspheroidized (red arrows: pores) and (**b**) spheroidized TiC powder.

In Figure 1a,b, the powder is demonstrated to have successfully spheroidized. The spheroidization of TiC powder was carried out in order to have the TiC and $AlSi_{10}Mg$ powder in the same morphology for AM characteristics. Figure 2a shows that little TiC is detected in the EDS. In fact, an amount of 0.04% titanium is observed. This could be due to the fact that TiC powder particles were unevenly distributed through a large amount of $AlSi_{10}Mg$ powder, leading to a lower Ti content detected [29]. During point detection, TiC is not picked up at all. This could possibly be a consequence of EDS detection limitations, which are the result of low concentrations of elements, particularly if the element is within a large matrix of $AlSi_{10}Mg$ [30,31]. Figure 2b shows that 2 wt.% TiC is detected in points 1 and 2. In point 1, it is observed that the TiC particle comprises a bumpy surface relative to the particles where aluminium is detected. In the EDS spectra, the presence of Ti is similarly recognised, although no carbon is distinguished. A percentage of 1.74% of Ti is detected with 98.26% aluminium, which is the major component. Carbon appears to have reacted with aluminium and other elements to form Al_4C_3, and again, carbon is too light an element to be detected by EDS, particularly if present in small amounts in complex compounds [31]. Contaminants of oxide particles like Al_2O_3 must have catalysed the reaction of Al and C [32]. It can be said that the undetected 0.22% is for the carbon because of the partial decomposition of TiC. Figure 2c shows 3 wt.% where lots of carbon is present in the micrographs points, and also, the EDS spectra demonstrate the presence of both carbon and titanium elements. A substantial amount of carbon existed in the percentage of 0.10% with 2.28% titanium. It is noticeable that an increase in TiC content is then able to be sufficiently picked up by the EDS system. In Figure 2d, 4 wt.% TiC is detected at point 1 of the micrograph. The bumpy surface is again observed in this particle. The presence of TiC is also evident in the EDS graph. The existence of Ti and carbon percentages in the 4% TiC mixture is confirmed to be 2.26% and 1.39%, respectively. In Figure 2e, the presence of 5 wt.% TiC is indicated at point 1 of the SEM image. Similarly, the EDS spectra confirmed the presence of titanium but not carbon. The percentage of Ti obtained is 1.29%, while no carbon is detected. A large quantity of 91.30 wt.% aluminium and 7.41 wt.% silicon is also observed. In the additive manufacturing procedures, the extremely restricted melting and solidification of metallic alloy powder that takes place in the additive manufacturing procedure is known to be sensitive to defects.

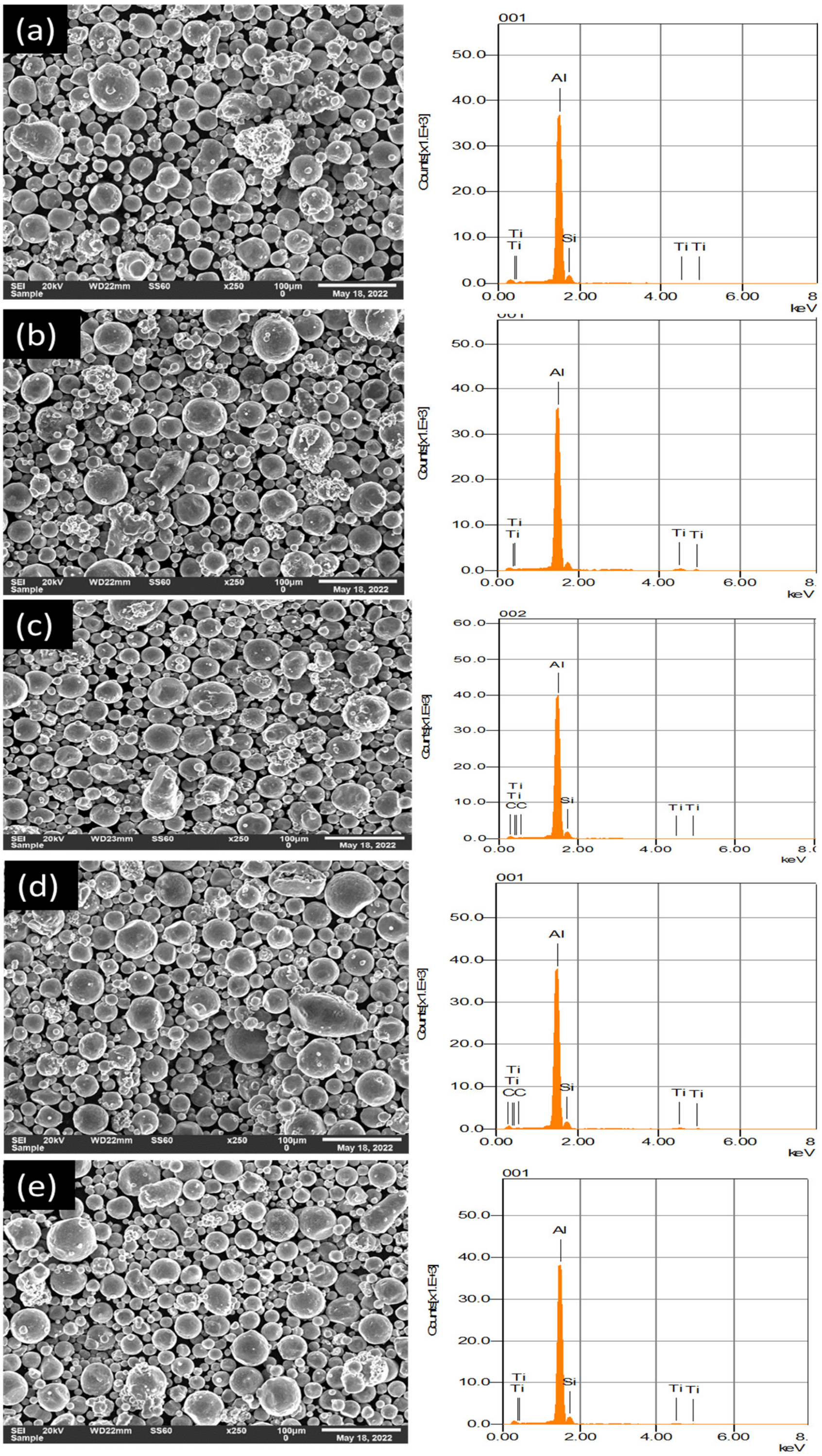

Figure 2. SEM microstructure and EDS of 1–5 wt.% TiC mixed in $AlSi_{10}Mg$, (**a**) 1 wt.%, (**b**) 2 wt. %, (**c**) 3 wt.%, (**d**) 4 wt.% and (**e**) 5 wt.%.

3.2. Thermogravimetric Analysis (TGA) of the Mixed $AlSi_{10}Mg$ with TiC Powders

According to Mfusi et al., $AlSi_{10}Mg$ powders gain weight until before the melting point of 596 °C. However, due to the ability of aluminium to form an oxide protective layer, the powder continues to gain weight and withstand temperatures of up to 800 °C. Figure 3 shows the $AlSi_{10}Mg$ powders mixed with 1–5 wt.% TiC powders.

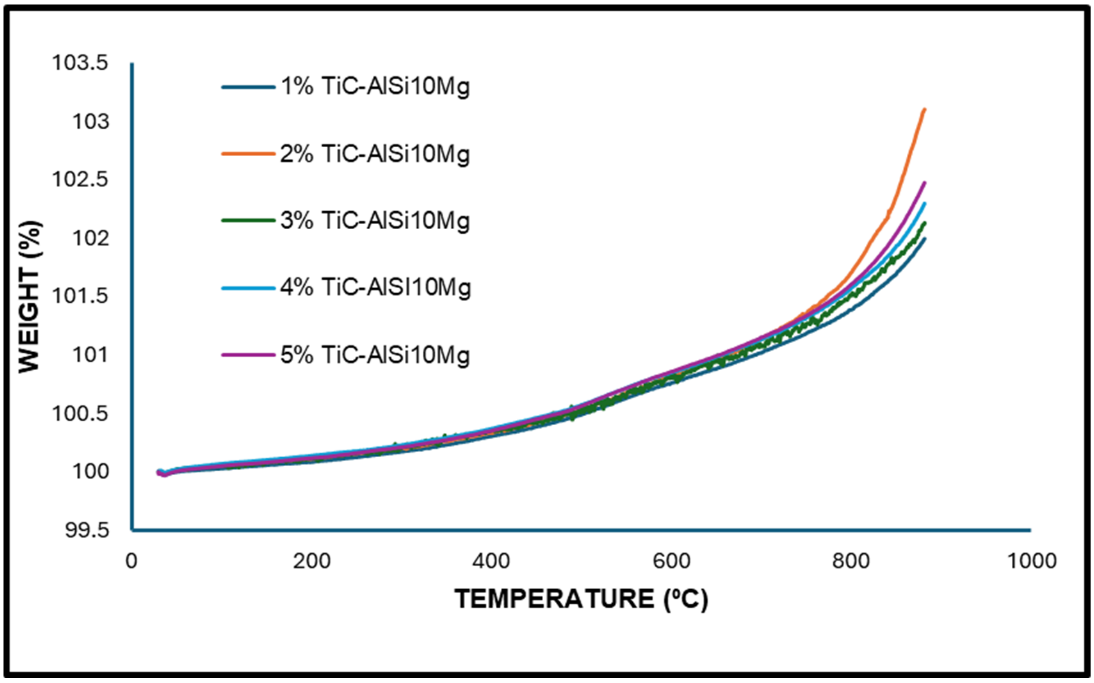

Figure 3. Thermogravimetric analysis results of the mixed TiC and $AlSi_{10}Mg$ powders.

After the addition of 1 wt.% TiC powders into the $AlSi_{10}Mg$, it was observed that the powder does not decompose at the melting point of aluminium of 596 °C [9]. TiC acts as a nucleation agent; a significantly small amount can impact TGA of $AlSi_{10}Mg$ due to its high thermodynamic stability and barrier properties [33]. It continued to increase in weight and tolerate higher temperatures, though it was stopped at 900 °C. At 2 wt.% TiC, the graph shows steepness followed by the 5 wt.% TiC graphs, while the rest are simply gradually going up. It was expected for the 5 wt.% TiC graph to go higher than the rest, followed by the 4 wt.% TiC. This is because a higher content of TiC can result in higher oxidation [34]. Furthermore, an increase in TiC can cause more complex reaction kinetics with multiple reactions occurring simultaneously, resulting in a noise signal, as observed in the 3 wt.% TiC graph [35]. The reaction with oxygen leads to the formation of the protective oxide layer, which may slow down further reactions, thus causing noisy data [36]. However, it is common knowledge that aluminium also reacts with oxygen to form aluminium oxide, leading to a mass increase. Magnesium can also do react, forming magnesium oxide, contributing to the protective oxide layer, which is observed in the 2 wt.% TiC sample. This signifies enhanced corrosion resistance and thermal stability characteristics, which are relevant for AlSi10 PBF processing [37,38].

3.3. Pycnometer Density Measurements of $AlSi_{10}Mg$/TiC Powder

Figure 4 represents the powder density of $AlSi_{10}Mg$ powders mixed with TiC from 1 to 5 wt.%. This was completed for the observation of the TiC powder effect on the $AlSi_{10}Mg$ density in terms of additive manufacturing process characteristics. The density of commercial $AlSi_{10}Mg$ is 2.65 g/cm^3 [9,39]. These as-received $AlSi_{10}Mg$ powder densities correspond to the densities in the literature of relative materials [1,12,16].

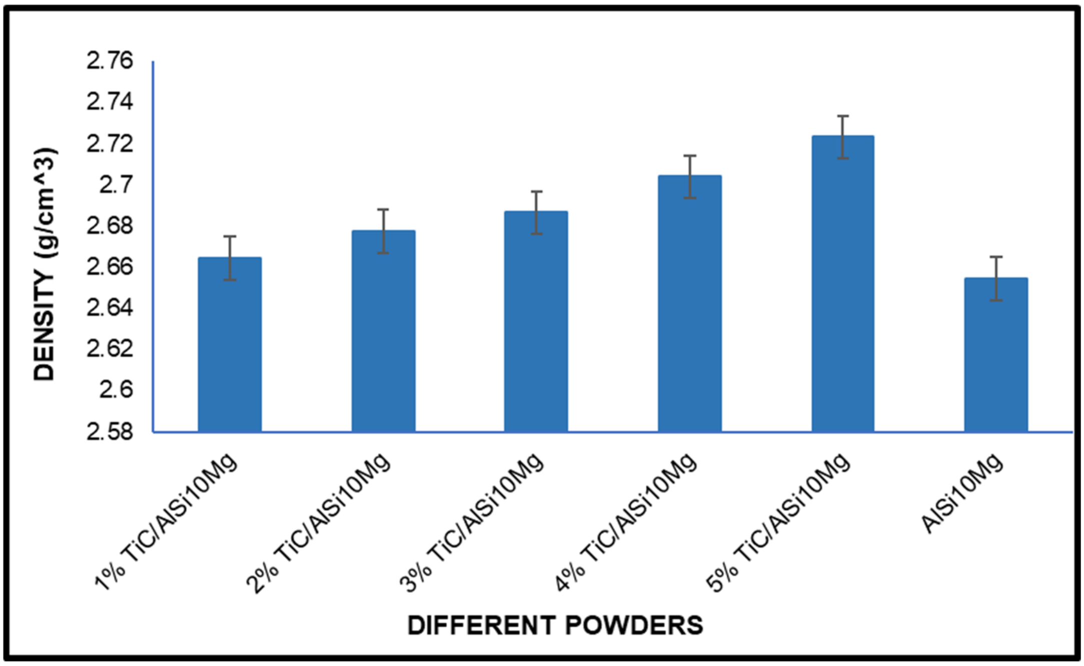

Figure 4. Density results of pure $AlSi_{10}Mg$ and TiC mixed in $AlSi_{10}Mg$ powder.

Figure 4 shows a reasonable distribution of TiC powder to $AlSi_{10}Mg$ powder, as direct proportionality is observed with the percentage increase in TiC powder. It is visibly demonstrated that pure TiC has more density than pure $AlSi_{10}Mg$. This was a result of titanium (Ti) and carbon (C) atoms' strong covalent bond, as well as the fact that titanium has a bigger atomic mass than aluminium, which was 47.87 g/mol and 26.98 g/mol, respectively [40]. TiC also had an FCC crystal structure, which is denser than that of $AlSi_{10}Mg$ in terms of atomic arrangement [41]. The percentage increase observed is 0.38% (1 wt.% TiC), 0.87% (2 wt.% TiC), 1.21% (3 wt.% TiC), 1.87% (4 wt.% TiC), and 2.60% (5 wt.% TiC) relative to the density of $AlSi_{10}Mg$. This increase in powder density may result in increased density of the resultant component, which will efficiently influence the mechanical characteristics such as hardness and strength [42,43]. This was the expected objective required in anticipation of solving the eutectic silicon network agglomeration problem during thermal treatment, which leads to the hardness and strength of the material being compromised [13]. An increase in powder density is also known for constant layer deposition during the PBF process as a result of enhanced powder flowability, as well as reduced porosity [44,45].

3.4. X-Ray Diffraction (XRD) of $AlSi_{10}Mg$/TiC Powder

$AlSi_{10}Mg$ is a widely used aerospace-grade material, with stringent industry standards such as ASTM B209 [46]. XRD characterisation was carried out to identify phases and the presence of TiC in each percentage mixture from 1 to 5 wt.%, exposing any changes in the crystal structure, lattice parameters, or crystal orientation as a result of powder mixing.

Figure 5 demonstrates that the powders have the same intensities, which means they possess the same crystal structure with high intensity at 40 to 45 degrees. The peaks of 40°, 45°, 65°, and 78° had been identified to be aluminium in their FCC atomic arrangement and are comparable to the (111), (200), (220), and (311) planes, respectively [16,47,48]. The FCC atomic arrangement is significant for AM processing for the same reason mentioned in 4.3.3, which is improved thermal characteristics [49]. It is significant for reducing hot tearing during AM processing, optimised corrosion resistance, as well as enhancing the microstructure [50]. The FCC atomic arrangement of $AlSi_{10}Mg$/TiC also achieves the objective of an outstanding strength-to-weight ratio, ductility, and fatigue resistance. This is because it enables the effective use of space and high atomic packing density, which leads to solid interatomic bonds and high strength [49,51].

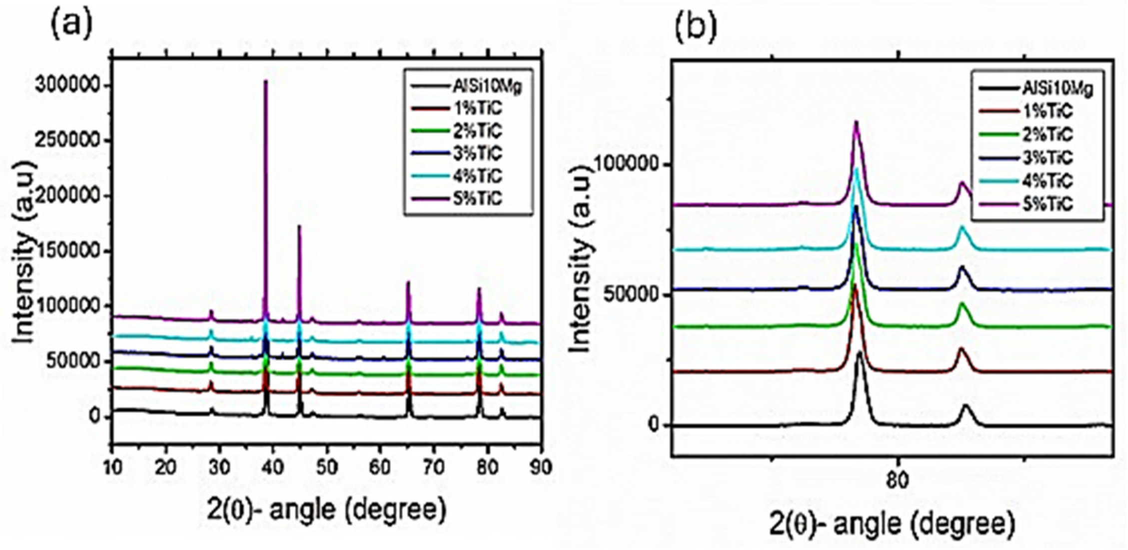

Figure 5. XRD results of AlSi$_{10}$Mg/TiC mixed powders and AR-AlSi$_{10}$Mg with (**a**) full spectra and (**b**) reduced spectra to demonstrate peak shifts with the change in TiC composition.

3.5. BET Surface Area Analysis of AlSi$_{10}$Mg/TiC Powder

The Brauner, Emmett, and Teller (BET) analysis was performed on the samples in order to determine the effect of TiC on the specific (a) surface area and (b) porosity volume of the AlSi$_{10}$Mg powder. This is for the purpose of revealing the size and distribution of pores affecting the flow of powder, relative density, and the impact they will have on the AM processing method.

In Figure 6a, the surface area of the powder demonstrated an increase from 0.05 m^2/g at 1 wt.% AlSi$_{10}$Mg/TiC to 0.16 m^2/g at 3 wt.% AlSi$_{10}$Mg/TiC, and a decrease to 0.1 m^2/g for 4 and 5 wt.% AlSi$_{10}$Mg/TiC. These powders are within the range because the AM process acceptable surface area is 0.1–5 m^2/g according to ASTM B925-17 for aluminium-based alloy powders for AM processing [52]. According to the literature, the commercial AlSi$_{10}$Mg powder is within 0.15–0.3 m^2/g [53]. These surface areas are often associated with good flowability and can lead to good packing density for the final component [54,55]. Figure 5b demonstrated a significantly low pore volume of 0.00005 to 0.00008 m^3/g, where 3 wt.% AlSi$_{10}$Mg/TiC appears to have the highest pore volume. This is due to the higher surface area observed in the 3 wt.% AlSi$_{10}$Mg/TiC sample. Uniform powder density and low pore volume ensure consistent melting behaviour, which results in enhanced component characteristics and reduced process variability [56]. The drawback with such low pore volume is the sensitive powder handling during AM processing, which may lead to powder degradation and agglomeration [53]. The acceptable pore volume for critical structural components in aerospace applications is 0.5% and 2% for aesthetic aerospace components [57].

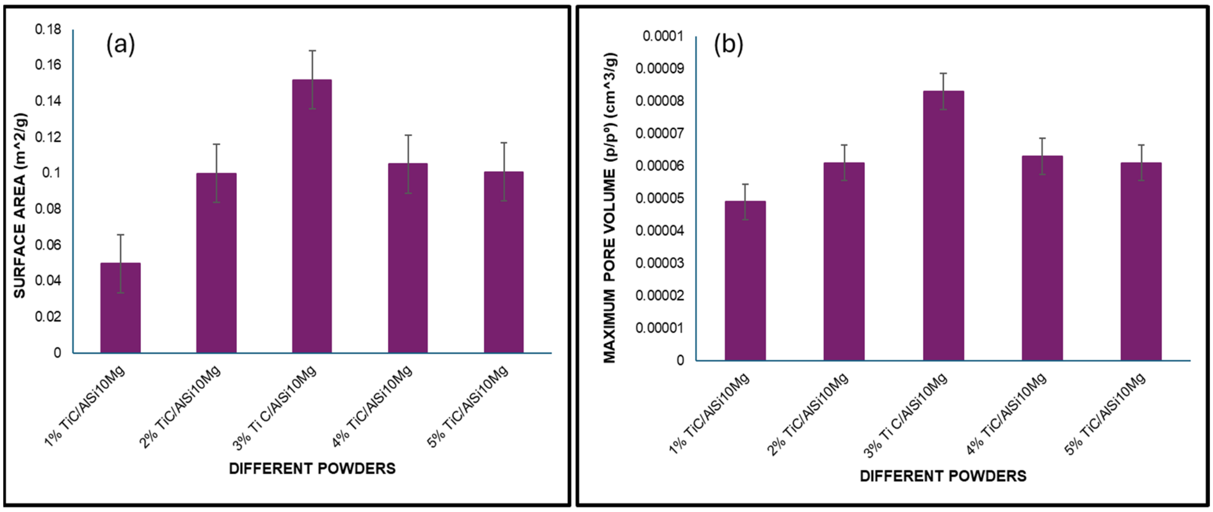

Figure 6. BET (**a**) surface area and (**b**) pore volume for $AlSi_{10}Mg/TiC$ mixed powders.

3.6. Modelling of Structural Mechanical Properties of the $AlSi_{10}Mg/TiC$ Powder

3.6.1. Lattice Structure of $AlSi_{10}Mg$ Mixed with TiC Powder

In Figure 7, the binary AlSi structure with the space group of Pm-3 m is shown. The supercell of a 2 × 2 × 2 AlSi structure with 16 atoms was generated, wherein Ti and C were substituted, i.e., $Al_{8-x}Si_8M_x$ (M: Ti, C). Modelling was conducted in order to understand the thermodynamic stability and interfacial characteristics, and to estimate the mechanical properties of $AlSi_{10}Mg$ reinforced with TiC from atomic-scale behaviour of the materials.

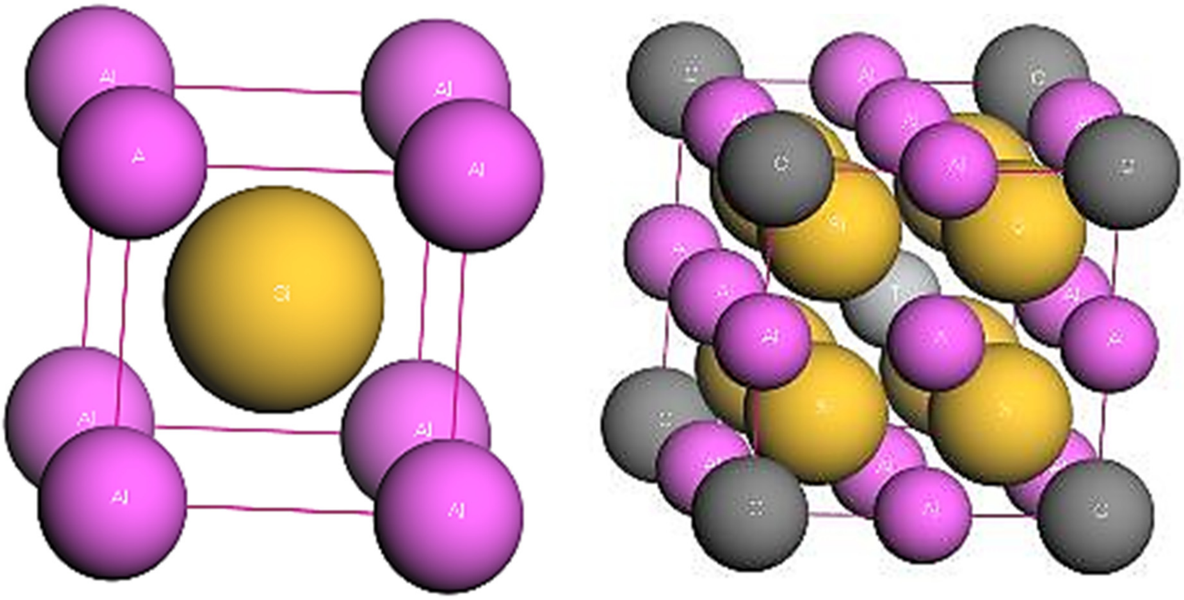

(**a**) (**b**)

Figure 7. The structures of beta (**a**) binary AlSi and (**b**) ternary AlSiTiC, where purple, orange, light grey, and dark grey represent Al, Si, Ti, and C, respectively.

In Figure 7b, the structure of the Al_6Si_8TiC ternary alloy is shown. The determined structures were optimised, and their equilibrium lattice parameters, density, and enthalpy of formation are shown in Table 1. It can be noted that the addition of both Ti and C reduces the lattice parameter of the AlSi structure, as depicted by the decreasing lattice parameters. The decrease is attributed to the difference in the atomic radius (Al (1.43), Ti (1.47), and C (0.914)) of atoms. This indicates that the combination of Ti and C alters the atomic arrangement, signifying that TiC is not an isolated phase but well incorporated at the atomic level into the matrix, possibly resulting in novel or improved material characteristics [48].

Table 1. The lattice parameters a, density ρ, and enthalpy H for the $Al_{8-x}Si_8M_x$ (M: Ti, C) structures.

Structure	**a (Å)**	**ρ (g/cm^3)**	**H (eV)**
AlSi	3.213	2.75574	−281
Al_7Si_8Ti	3.149	3.06563	−3730
Al_7 Si_8C	3.134	2.86889	−2290
Al_6Si_8TiC	3.103	3.10624	−3770

The reduction in the lattice parameter from 3.213 to 3.103 Å indicates a lattice contraction with the incorporation of TiC, which signifies an effective atomic-scale integration of Ti and C. Electron calculations and CASTEP simulations yielded identical predictions for the ground-state stable crystal structure of TiC embedded in AlSi matrix, collaborating the experimental results obtained from metallurgical investigations. According to Pankhurst et al., at ground-state, stable and metastable structures have a small energy gap. As the temperature increases above 0 Kelvin, entropy gains control and causes the metastable structure to appear in metallurgical experiments relative to the stable, expected one [58].

3.6.2. Enthalpy of Formation and Bulk Modulus of $AlSi_{10}Mg$ Mixed with TiC Powder

Figure 8 demonstrates the enthalpy of formation and bulk modulus of $AlSi_{10}Mg$ and TiC. The bulk modulus was measured by the application of hydrostatic pressure (P) to the material model. These are significant for determining the thermodynamical stability, flowability, and packing of the powder, as well as stress and cracking during AM processing.

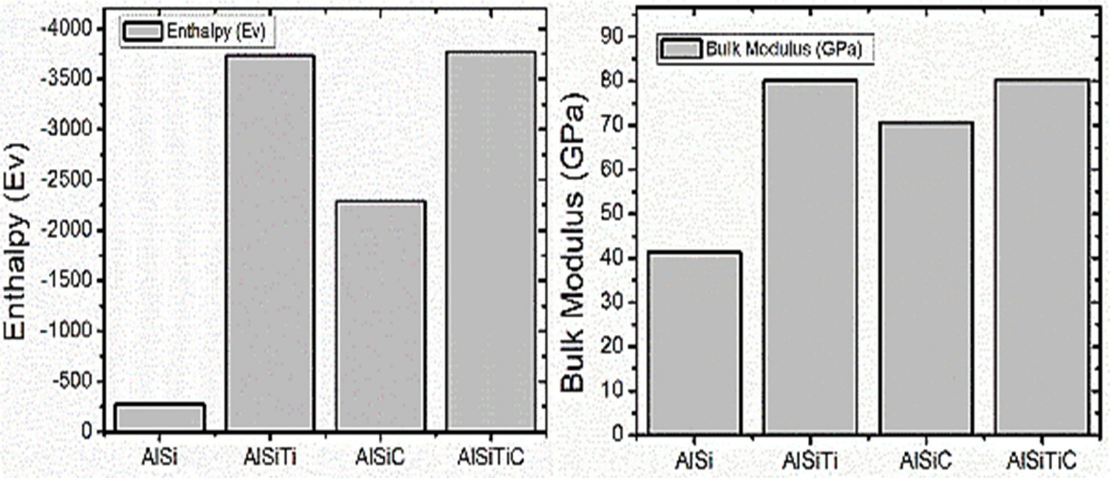

(**a**) (**b**)

Figure 8. The graphs of (**a**) enthalpy and (**b**) bulk modulus for the $Al_{8-x}Si_8M_x$ (M: Ti, C) structures.

In Figure 8a, an enthalpy graph against the structure is shown. Both Al_7Si_8Ti and Al_6Si_8TiC peaks are more negative than those of both AlSi and Al_7Si_8C, suggesting the stability of the structures. In Table 2, it can be clearly observed that Al_6Si_8TiC is the most stable structure with the lowest enthalpy of formation, which concurs with what is observed in the TGA results, Figure 3. More negative enthalpy indicates that the TiC-reinforced structure is much more stable thermodynamically. This signifies that TiC reinforcement of $AlSi_{10}Mg$ not only intensifies the strength of the matrix but also stabilises it, decreasing the risk of phase segregation throughout AM processing [59]. To further understand the ductility of the structures, the bulk modulus was calculated and plotted in Figure 8b. Ductility refers to the measure of a metal's ability to withstand tensile stress. The addition of Ti and C enhances the ductility of the AlSi alloy as denoted in the graph of Figure 8b. As Ti and C are added to the system, the bulk modulus increases, with Al_6Si_8TiC having the largest value of 80.34 GPa. This corresponds with what was observed on the non-atomic level above—that any slight addition of TiC in the $AlSi_{10}Mg$ powder improves the density of the alloy. The stable integration of TiC into the atomic structure and the lattice contraction indicate that it is improbable for the composite to undergo phase segregation during AM processing. It also indicates that the matrix is able to endure the rapid solidification and cooling AM cycles, with the reduction in cracking and distortion of components [60].

Table 2. The elastic constants of the $Al_{8-x}Si_8M_x$ (M: Ti, C) structures.

Structure	a = b = c (Å)	c11 (GPa)	c44 (GPa)	c12 (GPa)	C′ (GPa)	A (GPa)
AlSi	3.2134	−164	32	142	−153	−4.7813
Al_7Si_8Ti	6.2072	33.107	55.493	101.34	−34.118	−0.6148
Al_6Si_8TiC	6.2112	149.26	−195.51	57.875	45.695	−0.2337

3.6.3. The Density of State (DoS) of $AlSi_{10}Mg$ Mixed with TiC Powder

Figure 9 shows the Density of State (DoS) graphs for AlSiTi, AlSiC, and AlSiTiC as a function of energy E-Ef, which is the Fermi energy. These graphs were generated in order to compare the electronic structures of the materials when elements of TiC were added to AlSi. This impacts optical absorption, thermal conductivity, and melting behaviour of the powder during AM processing.

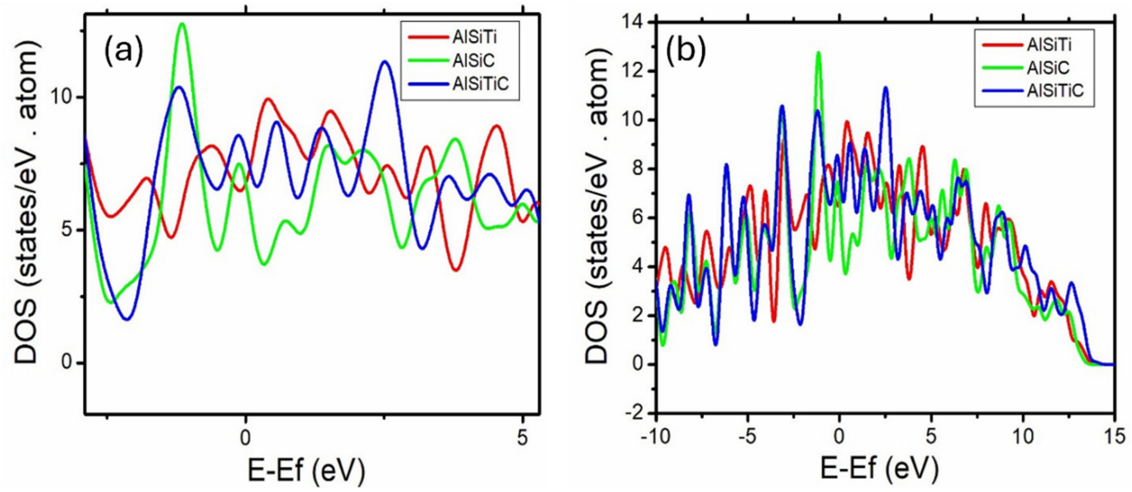

Figure 9. The Density of State (DoS) Fermi-level (**a**) full electronic spectrum and (**b**) metallicity spectrum for AlSiTi, AlSiC, and AlSiTiC.

The constituents observed in Figure 9 demonstrated metallic characteristics for all the compounds. The AlSiC has lower DoS at the Fermi level relative to AlSiTi and AlSiTiC, which signifies potentially low electric conductivity. Rapid heating and cooling factors, which govern the AM process, can sometimes result in non-equilibrium microstructures [61]. These electronic structural facts contribute to the understanding of the interaction of elements at an atomic level, the probability of establishing required and unwanted phases, as well as the stability of the processed structure throughout solidification, thus informing the processing parameters [62]. AlSiTiC proved to have the highest DoS at the Fermi level and at the peak above Ef. This demonstrated the powder's upgraded thermal stability, mechanical characteristics, porosity reduction and density increase, which are suitable for AM processing [63]. Interestingly, the addition of Ti and C increases the density of the alloy, with Ti contributing more to AlSi than C. The denser TiC intensifies the density of the composite completely, which is advantageous for hardness and wear resistance [64].

3.6.4. Density Function Theory (DFT): The Mechanical Characteristics of $AlSi_{10}Mg$ Mixed with TiC Powder

Figure 10 is the DFT simulation of Young's modulus, shear modulus and Poisson's ratio of AlSi and Al_6Si_8TiC as per the CASTEP modelling results. Determining this assists in relating the mechanical and elastic characteristics of the materials in simulation and experiment. Deformation resistance under shear stress is measured by shear modulus, signifying that the higher the shear modulus, the higher the deformation resistance [65]. Poisson's ratio defines the nature of bonding forces between atoms.

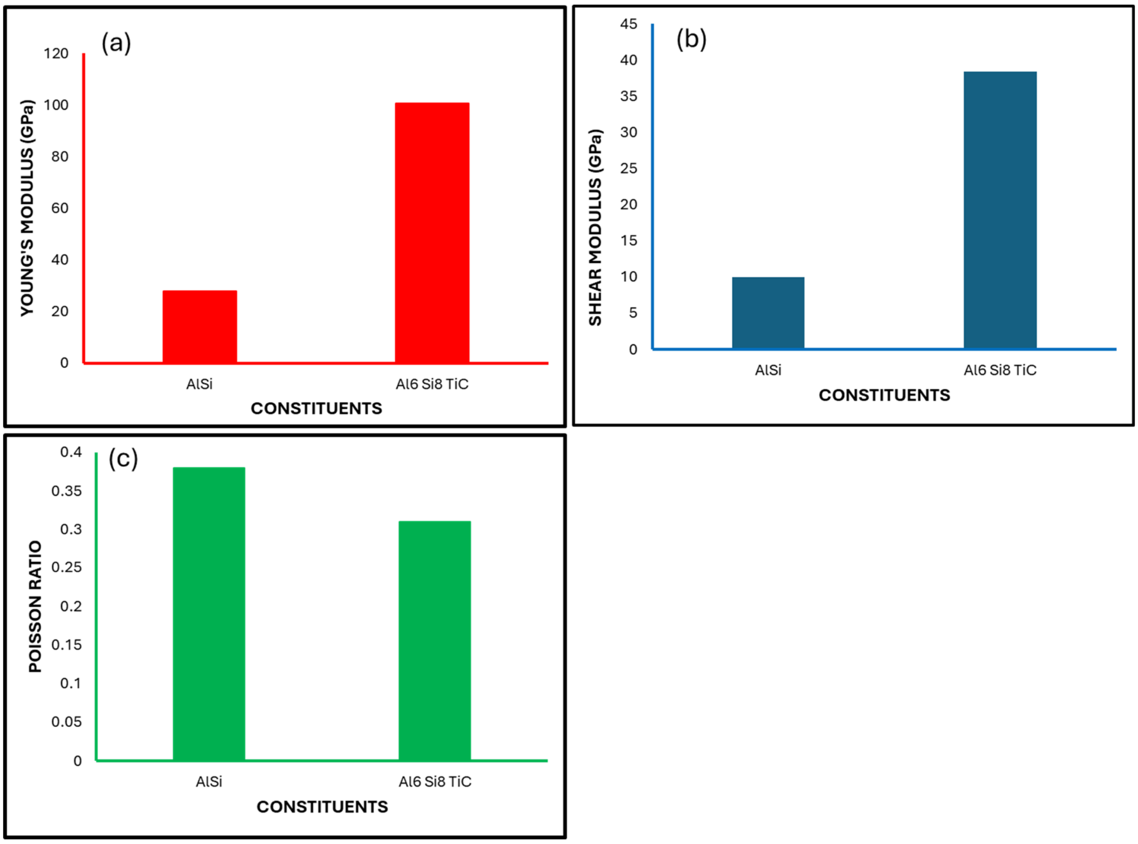

Figure 10. Mechanical characteristics. (**a**) Young's modulus, (**b**) shear modulus, and (**c**) Poisson's ratio of AlSi and Al_6Si_8TiC.

The graphs relate Young's modulus, shear modulus, and Poisson's ratio to important mechanical characteristics. It was observed that Young's modulus and shear modulus significantly increased with the addition of TiC into AlSi. This dramatic increase signifies that $AlSi_{10}Mg$ reinforcement with TiC substantially increases the stiffness and resistance to elastic deformation under tensile and compressive forces, and, when subjected to shear stress, signifies a significantly high resistance to change in shape [66,67]. Poisson's ratio was reduced with the addition of TiC. It is normal for most metals to show a positive Poisson's ratio. This is because of their metallic bonding characteristics and crystal lattice atomic structure [61,68]. This signifies that the material becomes stiffer, which is an indication of a more deformation-resistant material under stress [49,69]. Therefore, the variations in lattice parameters and elastic characteristics after the addition of TiC in AlSi have been precisely predicted by CASTEP's quantum modelling. This is in agreement with the improved extreme temperature oxidation resistance detected in the experimental investigations, Figure 3. Higher stability and density already point to mechanical improvements, like good wear resistance, increased strength and hardness and potentially refined microstructure, which are vital for AM component functionality [70,71]. These enhanced mechanical characteristics and stability indicate the suitability of TiC-reinforced $AlSi_{10}Mg$ for demanding rail, aerospace, and automotive industry AM applications.

Table 2 illustrates the elastic constants computed to investigate the mechanical stability of the structures. To determine the mechanical stability and elastic characteristics, the accuracy of calculating the elasticity is of vital importance in any system. The Born–Huang cubic crystal mechanical stability criteria equations are given [72].

$$C_{11} + 2C_{12} > 0,\ C_{11} - C_{12} > 0 \text{and } C_{44} > 0 \tag{1}$$

$$c' = \frac{(c_{11} - c_{12})}{2} \tag{2}$$

wherein:

$$A = \frac{2C_{44}}{C_{11} - C_{12}} \tag{3}$$

The stability criterion for the elastic constant must be fulfilled for the structure to be measured as stable. The C′ must be positive to indicate mechanical stability, according to the principle, as illustrated by Equations (1)–(3). As observed in Table 2, Al_6Si_8TiC is a positive 45.695 GPa, indicating that the addition of TiC to $AlSi_{10}Mg$ will harness a mechanically stable structure of the final component. The value of the total isotropy of a compound is 1 [73]. Values below and above 1 indicate that the compound exhibits anisotropic characteristics. In this case, Al_6Si_8TiC has an anisotropy value of -0.233, which indicates its degree of elastic anisotropy when built in certain directions [65].

4. Conclusions

- ○ The density increases significantly with the increasing TiC wt.% added to $AlSi_{10}Mg$ powder. An FCC aluminium phase was revealed, which is good for the strength-to-weight ratio of the final component.
- ○ An increased surface area is observed, especially in the powder with 3 wt.% TiC. It is concluded that the TiC mixture into the $AlSi_{10}Mg$ was well-distributed, as confirmed by the consistent increase in the density of the powder with the increase in the percentage mixture of TiC. The EDS analysis significantly demonstrated the presence of TiC in the different mixtures of 1–5 wt.%, even though the percentages of TiC present did not show an increasing trend similar to the density. This may be a consequence of the different characteristics exhibited by the different analyses.
- ○ The pore volume is significantly low, which is good for the final component packaging density, with a drawback for powder handling, which may result in powder degradation. However, the formation of the TiC metal–matrix composite has been determined to be a success due to the fact that the powder met the specifications for AM processing and aerospace applications.
- ○ CASTEP simulations demonstrated that TiC reinforcement of $AlSi_{10}Mg$ enhances the density of the alloy powder by contracting the lattice structure. This indicates enhanced powder flowability and final component density after AM processing.
- ○ Improved mechanical and thermal characteristics, which signify great thermodynamic stability, were demonstrated by the simulation. This indicates that the powder is oxidation-resistant at higher temperatures and has improved absorption and powder

consistency for AM processing. These results concur with the results demonstrated by the experimental investigation.

- ○ AlSiTiC demonstrated higher DoS for conduction, indicating improved electronic characteristics for applications requiring extreme conductivity. The effect of different atomic elements on the electronic structure of the materials was mirrored in the variation in the DoS profiles.
- ○ The increase in Young's and shear moduli indicated that adding TiC into AlSi alloys develops the hardness, stiffness, tensile strength, toughness, wear resistance, and grain refinement of the composite, rendering it extra fitting for severe applications. CASTEP has proven that improved mechanical characteristics with enhanced multiphase microstructures can be attained with the addition of TiC to Al-Si alloys.

Author Contributions: Conceptualization, N.R.M. and B.J.M.; writing—original draft preparation, B.J.M.; writing—review and editing, B.J.M. and N.R.M.; preparation and supervision, P.A.I.P.; TiC powder preparation, H.B.; atomic modelling, R.M. All authors have read and agreed to the published version of the manuscript.

Funding: The funding of the project was received from the South African Council of Science and Industrial Research, Department of Science and Innovation Collaborative Program on Additive Manufacturing and National Research Fund (Grant number: SRUG2204062372).

Data Availability Statement: The original contributions presented in this study are included in the article. Further inquiries can be directed to the corresponding author.

Acknowledgments: The authors would like to acknowledge the South African Council of Science and Industrial Research and Tshwane University of Technology; the Photonics Centre Metallurgical Laboratory and Advanced Materials & Manufacturing Metallurgical Testing facility; the CSIR/DSI Centre for Nanostructured Materials.

Conflicts of Interest: Author Hertzog Bisset was employed by the company South African Nuclear Energy Corporation SOC Ltd. The remaining authors declare that the research was conducted in the absence of any commercial or financial relationships that could be construed as a potential conflict of interest.

References

1. Du Plessis, A.; Glaser, D.; Moller, H.; Mathe, N.; Tshabalala, L.; Mfusi, B.; Mostert, R. Pore closure effect of laser shock peening of additively manufactured $AlSi_{10}Mg$. *3D Print. Addit. Manuf.* **2019**, *6*, 245–252. [CrossRef]
2. Aboulkhair, N.T. Additive Manufacture of an Aluminium Alloy: Processing, Microstructure, and Mechanical Properties. Ph.D. Thesis, University of Nottingham, Nottingham, UK, 2016.
3. Wohlers, T.; Gornet, T. *History of Additive Manufacturing (Wohlers Report 2014)*; Wohlers Associates, Inc.: Fort Collins, CO, USA, 2012.
4. Mozaffar, M.; Ndip-Agbor, E.; Lin, S.; Wagner, G.J.; Ehmann, K.; Cao, J. Acceleration strategies for explicit finite element analysis of metal powder-based additive manufacturing processes using graphical processing units. *Comput. Mech.* **2019**, *64*, 879–894. [CrossRef]
5. Zhou, S.; Wang, Z.Y.; Su, Y.; Wang, H.; Liu, G.; Song, T.T.; Yan, M. Effects of micron/submicron TiC on additively manufactured $AlSi_{10}Mg$: A comprehensive study from computer simulation to mechanical and microstructural analysis. *JOM* **2020**, *72*, 3693–3704.
6. Chu, F.; Zhang, K.; Shen, H.; Liu, M.; Huang, W.; Zhang, X.; Liang, E.; Zhou, Z.; Lei, L.; Hou, J.; et al. Influence of satellite and agglomeration of powder on the processability of $AlSi_{10}Mg$ powder in Laser Powder Bed Fusion. *J. Mater. Res. Technol.* **2021**, *11*, 2059–2073. [CrossRef]
7. Lekoadi, P.M.; Tlotleng, M.; Masina, B.N. Effects of substrate heating on the microstructure and hardness of TiB/Ti6Al4V-ELI during laser in-situ metal deposition. *Suid-Afr. Tydskr. Natuurwet. Tegnol.* **2021**, *40*, 60–65. [CrossRef]
8. Bagherifard, S.; Beretta, N.; Monti, S.; Riccio, M.; Bandini, M.; Guagliano, M. On the fatigue strength enhancement of additive manufactured $AlSi_{10}Mg$ parts by mechanical and thermal post-processing. *Mater. Des.* **2018**, *145*, 28–41.

9. Mfusi, B.J.; Mathe, N.R.; Popoola, P.A.I.; Tshabalala, L.C. Influence of stress relieving thermal cycles on AISI10Mg specimens produced by selective laser melting. In *IOP Conference Series: Materials Science and Engineering*; IOP Publishing: Bristol, UK, 2019.
10. Vasamsetti, S.; Dumpala, S.V.L. Synthesis, Characterization and Hardness Studies of Nano Rice Husk Ash Reinforced Al6061 Nanocomposites. *J. Eng. Sci. Technol.* **2018**, *13*, 2916–2929.
11. Staiano, G.; Gloria, A.; Ausanio, G.; Lanzotti, A.; Pensa, C.; Martorelli, M. Experimental study on hydrodynamic performances of naval propellers to adopt new additive manufacturing processes. *Int. J. Interact. Des. Manuf. (IJIDeM)* **2018**, *12*, 1–14. [CrossRef]
12. Mfusi, B.; Tshabalala, L.C.; Popoola, P.A.I.; Mathe, N.R. The effect of selective laser melting build orientation on the mechanical properties of $AlSi_{10}Mg$ parts. In *IOP Conference Series: Materials Science and Engineering*; IOP Publishing: Bristol, UK, 2018.
13. Mfusi, B.J.; Mathe, N.R.; Tshabalala, L.C.; Popoola, P.A. The effect of stress relief on the mechanical and fatigue properties of additively manufactured $AlSi_{10}Mg$ parts. *Metals* **2019**, *9*, 1216. [CrossRef]
14. Mfusi, B.J.; Mathe, N.R.; Motibane, L.; Glaser, D.; Lopez-Botello, O.E.; Popoola, P.A. The effect of T6 and hot isostatic pressure thermal treatments on the crack fatigue growth and fracture toughness of $AlSi_{10}Mg$ produced by additive manufacturing. *J. Manuf. Process.* **2025**, *151*, 1042–1057. [CrossRef]
15. Melendez, I.M.; Neubauer, E.; Angerer, P.; Danninger, H.; Torralba, J. Influence of nano-reinforcements on the mechanical properties and microstructure of titanium matrix composites. *Compos. Sci. Technol.* **2011**, *71*, 1154–1162. [CrossRef]
16. Cabeza, M.; Feijoo, I.; Merino, P.; Pena, G.; Pérez, M.; Cruz, S.; Rey, P. Effect of high energy ball milling on the morphology, microstructure and properties of nano-sized TiC particle-reinforced 6005A aluminium alloy matrix composite. *Powder Technol.* **2017**, *321*, 31–43. [CrossRef]
17. Gan, Y.X. Effect of interface structure on mechanical properties of advanced composite materials. *Int. J. Mol. Sci.* **2009**, *10*, 5115–5134. [CrossRef] [PubMed]
18. Cai, R.; Jin, T. The effect of microstructure of unidirectional fibre-reinforced composites on mechanical properties under transverse loading: A review. *J. Reinf. Plast. Compos.* **2018**, *37*, 1360–1377. [CrossRef]
19. Munz, D.; Fett, T. *Ceramics: Mechanical Properties, Failure Behaviour, Materials Selection*; Springer Science & Business Media: Berlin/Heidelberg, Germany, 1999; Volume 36.
20. Gherrab, M.; Garnier, V.; Gavarini, S.; Millard-Pinard, N.; Cardinal, S. Oxidation behavior of nano-scaled and micron-scaled TiC powders under air. *Int. J. Refract. Met. Hard Mater.* **2013**, *41*, 590–596. [CrossRef]
21. Hong, S.-M.; Park, J.-J.; Park, E.-K.; Kim, K.-Y.; Lee, J.-G.; Lee, M.-K.; Rhee, C.-K.; Lee, J.K. Fabrication of titanium carbide nano-powders by a very high speed planetary ball milling with a help of process control agents. *Powder Technol.* **2015**, *274*, 393–401. [CrossRef]
22. Mathe, N.R.; Tshabalala, L.C. The validation of the microstructural evolution of selective laser-melted $AlSi_{10}Mg$ on the in-house built machine: Energy density studies. *Prog. Addit. Manuf.* **2019**, *4*, 431–442. [CrossRef]
23. Kohn, W.; Sham, L.J. Self-consistent equations including exchange and correlation effects. *Phys. Rev.* **1965**, *140*, A1133. [CrossRef]
24. Baerends, E. Perspective on "Self-consistent equations including exchange and correlation effects" Kohn W, Sham LJ (1965) Phys Rev A 140: 133–1138. *Theor. Chem. Acc.* **2000**, *103*, 265–269.
25. Clark, S.J.; Segall, M.D.; Pickard, C.J.; Hasnip, P.J.; Probert, M.I.J.; Refson, K.; Payne, M.C. First principles methods using CASTEP. *Z. Für Krist.-Cryst. Mater.* **2005**, *220*, 567–570. [CrossRef]
26. Blöchl, P.E. Projector augmented-wave method. *Phys. Rev. B* **1994**, *50*, 17953. [CrossRef]
27. Perdew, J.P. Accurate and simple analytic representation of the electron-gas correlation energy. *Phys. Rev. B* **1992**, *45*, 60. [CrossRef] [PubMed]
28. Monkhorst, H.J. Hartree-Fock density of states for extended systems. *Phys. Rev. B* **1979**, *20*, 1504. [CrossRef]
29. Wei, W.; Zhang, Q.; Wu, W.; Cao, H.; Shen, J.; Fan, S.; Duan, X. Agglomeration-free nanoscale TiC reinforced titanium matrix composites achieved by in-situ laser additive manufacturing. *Scr. Mater.* **2020**, *187*, 310–316. [CrossRef]
30. Attar, H.; Prashanth, K.G.; Zhang, L.-C.; Calin, M.; Okulov, I.V.; Scudino, S.; Yang, C.; Eckert, J. Effect of powder particle shape on the properties of in situ Ti–TiB composite materials produced by selective laser melting. *J. Mater. Sci. Technol.* **2015**, *31*, 1001–1005. [CrossRef]
31. Qian, M. Metal powder for additive manufacturing. *JOM* **2015**, *67*, 536–537. [CrossRef]
32. Neyt, N.C.; Riley, D.L. Application of reactor engineering concepts in continuous flow chemistry: A review. *React. Chem. Eng.* **2021**, *6*, 1295–1326. [CrossRef]
33. Sun, X.; Zou, S.; Wang, F.; Gao, M.; Zhang, K.; Liu, T.; Zhu, Z.; Lu, W.; Liao, W. Role of TiC on the microstructure, tensile property and thermal stability of laser powder bed fusion fabricated $AlSi_{10}Mg$ alloy. *Mater. Sci. Eng. A* **2024**, *915*, 147182. [CrossRef]
34. Shimada, S. A thermoanalytical study of oxidation of TiC by simultaneous TGA-DTA-MS analysis. *J. Mater. Sci.* **1996**, *31*, 673–677. [CrossRef]
35. Saba, F.; Zhang, F.; Liu, S.; Liu, T. Reinforcement size dependence of mechanical properties and strengthening mechanisms in diamond reinforced titanium metal matrix composites. *Compos. Part B Eng.* **2019**, *167*, 7–19. [CrossRef]

36. Koc, R. Kinetics and phase evolution during carbothermal synthesis of titanium carbide from carbon-coated titania powder. *J. Eur. Ceram. Soc.* **1997**, *17*, 1309–1315. [CrossRef]
37. Minhas, N.; Sharma, V.; Bhadauria, S.S. A review on weldability and corrosion behaviour of L-PBF printed $AlSi_{10}Mg$ alloy. *Can. Metall. Q.* **2023**, *62*, 262–294. [CrossRef]
38. Cabrini, M.; Calignano, F.; Fino, P.; Lorenzi, S.; Lorusso, M.; Manfredi, D.; Testa, C.; Pastore, T. Corrosion behavior of heat-treated $AlSi_{10}Mg$ manufactured by laser powder bed fusion. *Materials* **2018**, *11*, 1051. [CrossRef] [PubMed]
39. Trinchieri, I. Re-Design in $AlSi_{10}Mg$ Alloy of an ICE Piston for SLM Process. Master's Thesis, Politecnico di Torino, Torino, Italy, 2023.
40. Levy, A.; Miriyev, A.; Elliott, A.; Babu, S.S.; Frage, N. Additive manufacturing of complex-shaped graded TiC/steel composites. *Mater. Des.* **2017**, *118*, 198–203. [CrossRef]
41. Gu, D.; Wang, H.; Dai, D.; Chang, F.; Meiners, W.; Hagedorn, Y.-C.; Wissenbach, K.; Kelbassa, I.; Poprawe, R. Densification behavior, microstructure evolution, and wear property of TiC nanoparticle reinforced $AlSi_{10}Mg$ bulk-form nanocomposites prepared by selective laser melting. *J. Laser Appl.* **2015**, *27*, S17003. [CrossRef]
42. Xu, R.; Li, R.; Yuan, T.; Zhu, H.; Li, P. Microstructure and mechanical properties of TiC-reinforced Al–Mg–Sc–Zr composites additively manufactured by laser direct energy deposition. *Acta Metall. Sin. (Engl. Lett.)* **2022**, *35*, 411–424. [CrossRef]
43. Hamilton, J. Additive Manufacturing Materials: Fabrication of Aluminum Matrix Composites. Master's Thesis, Rochester Institute of Technology, Rochester, NY, USA, 2019.
44. Gao, C.; Wu, W.; Shi, J.; Xiao, Z.; Akbarzadeh, A. Simultaneous enhancement of strength, ductility, and hardness of TiN/$AlSi_{10}Mg$ nanocomposites via selective laser melting. *Addit. Manuf.* **2020**, *34*, 101378. [CrossRef]
45. Raj Mohan, R.; Venkatraman, R.; Raghuraman, S.; Kumar, P.M.; Rinawa, M.L.; Subbiah, R.; Arulmurugan, B.; Rajkumar, S. Processing of Aluminium-Silicon Alloy with Metal Carbide as Reinforcement through Powder-Based Additive Manufacturing: A Critical Study. *Scanning* **2022**, *2022*, 5610333. [CrossRef]
46. Shakil, S.; Hadadzadeh, A.; Amirkhiz, B.S.; Pirgazi, H.; Mohammadi, M.; Haghshenas, M. Additive manufactured versus cast $AlSi_{10}Mg$ alloy: Microstructure and micromechanics. *Results Mater.* **2021**, *10*, 100178. [CrossRef]
47. Ayieko, C.O.; Musembi, R.; Ogacho, A.; Aduda, B.; Muthoka, B.; Jain, P. Controlled texturing of aluminum sheet for solar energy applications. *Adv. Mater. Phys. Chem.* **2015**, *5*, 458–466. [CrossRef]
48. Zhang, H.; Maljkovic, N.; Mitchell, B.S. Structure and interfacial properties of nanocrystalline aluminum/mullite composites. *Mater. Sci. Eng. A* **2002**, *326*, 317–323. [CrossRef]
49. Li, Y.; Zhang, D.; Wang, H.; Cong, W. Fabrication of a TiC-Ti matrix composite coating using ultrasonic vibration-assisted laser directed energy deposition: The effects of ultrasonic vibration and TiC content. *Metals* **2021**, *11*, 693. [CrossRef]
50. Rubben, T.; Revilla, R.I.; De Graeve, I. Influence of heat treatments on the corrosion mechanism of additive manufactured $AlSi_{10}Mg$. *Corros. Sci.* **2019**, *147*, 406–415. [CrossRef]
51. Lam, L.; Zhang, D.; Liu, Z.; Chua, C. Phase analysis and microstructure characterisation of $AlSi_{10}Mg$ parts produced by Selective Laser Melting. *Virtual Phys. Prototyp.* **2015**, *10*, 207–215. [CrossRef]
52. Moreira, F.; Ferreira, P.M.; Silva, R.J.C.; Santos, T.G.; Vidal, C. Aluminium-based dissimilar alloys surface composites reinforced with functional microparticles produced by upward friction stir processing. *Coatings* **2023**, *13*, 962. [CrossRef]
53. Balbaa, M.; Ghasemi, A.; Fereiduni, E.; Elbestawi, M.; Jadhav, S.; Kruth, J.-P. Role of powder particle size on laser powder bed fusion processability of $AlSi_{10}Mg$ alloy. *Addit. Manuf.* **2021**, *37*, 101630. [CrossRef]
54. Di Egidio, G.; Ceschini, L.; Morri, A.; Zanni, M. Room-and High-Temperature Fatigue Strength of the T5 and Rapid T6 Heat-Treated $AlSi_{10}Mg$ Alloy Produced by Laser-Based Powder Bed Fusion. *Metals* **2023**, *13*, 263. [CrossRef]
55. Ekaputra, C.N.; Weiss, D.; Mogonye, J.-E.; Dunand, D.C. Eutectic, precipitation-strengthened alloy via laser fusion of blends of Al-7Ce-10Mg (wt.%), Zr, and Sc powders. *Acta Mater.* **2023**, *246*, 118676. [CrossRef]
56. Hastie, J.C.; Kartal, M.E.; Carter, L.N.; Attallah, M.M.; Mulvihill, D.M. Classifying shape of internal pores within $AlSi_{10}Mg$ alloy manufactured by laser powder bed fusion using 3D X-ray micro computed tomography: Influence of processing parameters and heat treatment. *Mater. Charact.* **2020**, *163*, 110225. [CrossRef]
57. Davis, J.R. *Surface Engineering for Corrosion and Wear Resistance*; ASM International: Almere, The Netherlands, 2001.
58. Pankhurst, D.; Nguyen-Manh, D.; Pettifor, D. Electronic origin of structural trends across early transition-metal disilicides: Anomalous behavior of $CrSi_2$. *Phys. Rev. B* **2004**, *69*, 075113. [CrossRef]
59. Meijun, L.; Xu, L.; Zhu, C.; Li, Z.; Wei, S. Research progress of high entropy alloy: Surface treatment improves friction and wear properties. *J. Mater. Res. Technol.* **2024**, *28*, 752–773.
60. Huang, L.; Zhou, X. DFT predicting structural stability of Li-doped Al-Li solid solution using first principles. *J. Phys. Conf. Ser.* **2023**, *2639*, 012013.
61. Li, B.-Q.; Li, Z.; Bai, P.; Liu, B.; Kuai, Z. Research on surface roughness of $AlSi_{10}Mg$ parts fabricated by laser powder bed fusion. *Metals* **2018**, *8*, 524.

62. Wang, P.; Eckert, J.; Prashanth, K.-G.; Wu, M.-W.; Kaban, I.; Xi, L.-X.; Scudino, S. A review of particulate-reinforced aluminum matrix composites fabricated by selective laser melting. *Trans. Nonferrous Met. Soc. China* **2020**, *30*, 2001–2034. [CrossRef]
63. Prashanth, K.; Eckert, J. Formation of metastable cellular microstructures in selective laser melted alloys. *J. Alloys Compd.* **2017**, *707*, 27–34.
64. Wang, C.; Gong, Y.; Liu, B.; Fu, K.; Yao, Y.; Hitz, E.; Li, Y.; Dai, J.; Xu, S.; Luo, W.; et al. Conformal, nanoscale ZnO surface modification of garnet-based solid-state electrolyte for lithium metal anodes. *Nano Lett.* **2017**, *17*, 565–571. [CrossRef]
65. Mathews, T.; Sithole, E.; Modiba, R.; Madigoe, M. Study of shape memory properties of $Ti_{(50)}Ni_{(50-x)}M_x$ (M = Nb, Mo and Fe) alloys for biomedical applications using first principle approach. In *MATEC Web of Conferences*; EDP Sciences: Les Ulis, France, 2023.
66. Kumar, G.S.P.; Koppad, P.G.; Keshavamurthy, R.; Alipour, M. Microstructure and mechanical behaviour of in situ fabricated AA6061-TiC metal matrix composites. *Arch. Civ. Mech. Eng.* **2017**, *17*, 535–544.
67. Prasad, S.; Asthana, R. Aluminum metal-matrix composites for automotive applications: Tribological considerations. *Tribol. Lett.* **2004**, *17*, 445–453. [CrossRef]
68. Ledbetter, H.; Migliori, A. A general elastic-anisotropy measure. *J. Appl. Phys.* **2006**, *100*, 063516. [CrossRef]
69. Liu, Y.; Liu, C.; Liu, W.; Ma, Y.; Tang, S.; Liang, C.; Cai, Q.; Zhang, C. Optimization of parameters in laser powder deposition $AlSi_{10}Mg$ alloy using Taguchi method. *Opt. Laser Technol.* **2019**, *111*, 470–480.
70. Diniță, A.; Neacșa, A.; Portoacă, A.I.; Tănase, M.; Ilinca, C.N.; Ramadan, I.N. Additive manufacturing post-processing treatments, a review with emphasis on mechanical characteristics. *Materials* **2023**, *16*, 4610. [CrossRef] [PubMed]
71. Jiang, X.; Lu, J.; Zhao, N.; Chen, Z.; Zhao, Z. A review of wear in additive manufacturing: Wear Mechanism, Materials, and Process. *Lubricants* **2024**, *12*, 321. [CrossRef]
72. Colinet, C.; Tedenac, J.-C. Enthalpies of formation of TM–X compounds (X = Al, Ga, Si, Ge, Sn). Comparison of ab-initio values and experimental data. *Calphad* **2016**, *54*, 16–34. [CrossRef]
73. Baloyi, M.; Modiba, R.; Ngoepe, P.E.; Chauke, H.R. Structural elastic and electronic properties of binary titanium-based shape memory alloys. In Proceedings of the South African Institutes of Physics (SAIP), Bloemfontein, South Africa, 25–29 June 2018.